Reentrant Hexagons in non-Boussinesq Convection

By Santiago Madruga†, Hermann Riecke†, and Werner Pesch‡

†Department of Engineering Sciences and Applied Mathematics, Northwestern University, Evanston, IL 60208, USA

‡Physikalisches Institut, Universität Bayreuth, D-95440 Bayreuth, Germany

(Received 16th October 2004)

The stability and dynamics of hexagonal patterns is analyzed numerically in strongly nonlinear non-Boussinesq convection. The fluid parameters correspond to those of water, with emphasis on realistic experimental conditions. The stability analysis of the spatially periodic solution is performed with a Galerkin approach allowing arbitrary perturbations. The temporal evolution of the patterns is studied for periodic boundary conditions and for conditions corresponding to a circular container. While hexagons are known to be stable close to threshold (i.e. for Rayleigh numbers $R \approx R_c$) it has been commonly assumed that quite generally they become unstable to rolls already for slightly higher Rayleigh numbers and remain unstable as the Rayleigh number is increased. In contrast we find that depending on the strength of the non-Boussinesq effects the hexagons can restabilize again for larger Rayleigh numbers. For instance, hexagons that become unstable at $\epsilon \equiv (R - R_c)/R_c = 0.15$ can become stable again at $\epsilon = 0.2$. Direct simulations for circular containers show that these reentrant hexagons can prevail even for side-wall conditions that favor convection in the form of the competing stable rolls. For sufficiently strong non-Boussinesq effects hexagons are stable even over the whole R range considered, $0 \leq \epsilon \leq 1.5$. The reentrance of hexagons for larger R is attributed to the increase of the non-Boussinesq effects with Rayleigh number and the existence of stable hexagons in standard Boussinesq convection at larger Rayleigh numbers. These results provide insight into recent convection experiments using SF_6 in which reentrant hexagons were observed.

Contents

PACS numbers: 47.20.Dr, 47.20.Bp, 47.54.+r, 47.27.Te, 44.25.+f, 47.20.Ma

1 Introduction

Rayleigh-Bénard convection has served as an excellent paradigm for studying systems that spontaneously form spatial or spatio-temporal patterns (e.g. Bodenschatz *et al.* (2000)). In recent years exciting results have been obtained for the stability and dynamics

of structures that are connected with roll convection. To mention are, in particular, the spiral-defect chaos obtained in convection of fluids with low Prandtl number (Morris *et al.* (1993); Decker *et al.* (1994); Morris *et al.* (1996); Egolf *et al.* (2000); Matley *et al.* (2001); Chiam *et al.* (2003)) and domain chaos (Zhong & Ecke (1992); Bodenschatz *et al.* (1992); Hu *et al.* (1995, 1998)) driven by the Küppers-Lortz instability (Küppers & Lortz (1969)) in rotating systems. In most of these investigations great care has been taken to keep the experimental systems close to the regime in which the Oberbeck-Boussinesq approximation is valid by minimizing the dependence of the fluid parameter on the temperature in order to avoid the appearance of cellular or hexagonal structures.

It has long been recognized that variations of the fluid parameters with the temperature, i.e. non-Oberbeck-Boussinesq (NOB) effects, break a certain up-down symmetry and therefore introduce otherwise prohibited resonant-triad mode interactions. In one horizontal dimension this interaction involves the fundamental Fourier mode and its first harmonic. The interaction between these two modes can lead to traveling rolls and other dynamic phenomena even though the primary bifurcation giving rise to the patterns is a steady bifurcation (Dangelmayr (1986); Proctor & Jones (1988); Manogg & Metzener (1994); Prat *et al.* (2002)). In two horizontal dimensions various combinations of modes can interact through a resonant triad (cf. Proctor & Matthews (1996)). The best-studied case is the interaction among the three Fourier modes whose wavevectors form a hexagonal pattern. Due to the resonant interaction the primary bifurcation to the hexagons is transcritical and therefore the hexagons are preferred over rolls in the immediate vicinity of onset (Busse (1967)).

According to leading-order weakly nonlinear analysis, hexagons typically become unstable to rolls further above threshold where the amplitudes are larger and the resonant-triad interaction looses significance compared to interactions involving four modes (Palm (1960); Segel & Stuart (1962); Segel (1965); Busse (1967); Palm *et al.* (1967); Davis & Segel (1968)). This scenario of a transition from hexagons to rolls has been confirmed in quite a number of experimental investigations (Somerscales & Dougherty (1970); Dubois *et al.* (1978); Richter (1978); Walden & Ahlers (1981); Bodenschatz *et al.* (1991); Pampaloni *et al.* (1992)) and it has commonly been assumed that in convection hexagonal patterns are confined to the regime close to onset. Presumably due to this assumption, hexagonal convection in strongly nonlinear non-Boussinesq convection has not been investigated much.

Recently, however, two experiments showed that even in the strongly nonlinear regime stable hexagonal convection patterns can be observed. In one experiment hexagons were observed at relatively high Rayleigh numbers ($\epsilon \equiv (R - R_c)/R_c \approx 3.5$) under conditions, in which the Oberbeck-Boussinesq approximation was quite well satisfied (Assenheimer & Steinberg (1996)). In that case hexagons with up-flow and those with down-flow in the center are equivalent and both were observed to coexist in adjacent domains. A subsequent numerical stability analysis confirmed the existence of such stable OB-hexagons (Clever & Busse (1996); Busse *et al.* (1999)). They are characterized by an asymmmetry between rising and descending flows and a greater efficiency of the heat transport by the resulting plumes compared to symmetric two-dimensional roll convection. Since modes with higher wave-numbers contribute strongly to the asymmetry the phenomenon cannot be captured using cubic-order amplitude equations (Busse & Clever (1999)). In the other experiment a strongly non-Boussinesq situation was investigated and hexagons were observed not only close to threshold but also again as reentrant hexagons at higher Rayleigh numbers, $\epsilon = \mathcal{O}(1)$ (Roy & Steinberg (2002)). As the non-Boussinesq effects were increased the intermediate ϵ-range over which rolls were the preferred planform shrank and eventually hexagons were found to dominate rolls from onset all the way

to $\epsilon = \mathcal{O}(1)$. In the experiment the working fluid was SF_6 near its thermodynamical critical point and the restabilization of hexagons at larger ϵ was attributed to the high compressibility of SF_6 in this regime (Roy & Steinberg (2002)).

In previous numerical stability calculations of *rotating* non-Boussinesq convection in water we found that hexagons can be linearly stable over the whole range $0 \leq \epsilon \leq 1$ (Young *et al.* (2003)). In the strongly nonlinear regime $\epsilon = \mathcal{O}(1)$ we found a chaotic state ('whirling chaos') in which individual hexagonal cells oscillate or rotate, often inducing the nucleation of additional cells. Even in the presence of lateral walls, which typically induce the nucleation of rolls, this hexagon-based spatio-temporally chaotic state was found to persist. In that investigation the mechanism that is responsible for the linear stability of the hexagons over a fairly wide range in ϵ was, however, not understood.

In the present paper we identify easily accessible parameter regimes of non-Boussinesq convection in which strongly nonlinear hexagons are linearly stable. We point out two main mechanism which contribute to their stability. First, with increasing Rayleigh number the temperature difference across the fluid layer increases and with it the strength of the NOB-effects. A simple weakly nonlinear model shows that this effect alone can be sufficient to lead to a restabilization of the hexagons already at relatively low values of ϵ, which experimentally leads to reentrant hexagons. Second, the mechanism that stabilizes OB-hexagons at larger Rayleigh numbers also enhances the stability of the NOB-hexagons. Together, these two mechanism can lead to a restabilization for values of ϵ as low as $\epsilon = 0.2$. Since our computations are based on water as a working fluid (cf. Young *et al.* (2003)), which is essentially incompressible in the investigated regime, it is clear that high compressibility is not a necessary condition to obtain reentrant hexagons.

The paper is organized as follows. In Sec.2 we briefly review the basic equations that we use, pointing out in which way our computations are focusing on weakly non-Boussinesq, but strongly nonlinear convection. In Sec.3 we present our results for the linear stability regimes of hexagonal and roll patterns. The two mechanisms leading to restabilization are discussed in Sec.4. Direct simulations of the temporal evolution for boundary conditions mimicking circular containers are discussed in Sec.5. Conclusions follow in Sec.6.

2 Basic equations

We consider a horizontal fluid layer of thickness d, density ρ, kinematic viscosity ν, heat conductivity λ, and specific heat c_p. The layer is infinite in the horizontal extension and is limited in the vertical direction by two horizontal, rigid plates with high thermal conductivity. The system is heated from below (at temperature T_1) and cooled from above (at temperature $T_2 < T_1$). The governing equations expressing the balance of momentum, mass, and energy are (Chandrasekhar (1961))

$$\partial_t(\rho u_i) + \partial_j(\rho u_j u_i) = -\partial_i p - \rho g \delta_{i3} + \partial_j \left(\nu\rho \left(\partial_i u_j + \partial_j u_i\right)\right) \tag{2.1}$$

$$\partial_t \rho + \partial_j(\rho u_j) = 0 \tag{2.2}$$

$$\partial_t T + u_j \partial_j T = \frac{1}{\rho c_p} \partial_j(\lambda \partial_j T). \tag{2.3}$$

Here $\vec{u} = (u_1, u_2, u_3)$ is the fluid velocity, T the temperature, p the pressure, g the acceleration of gravity, and δ_{ij} is the Kronecker delta. Summation over repeated indices is implied. The origin of a Cartesian coordinate system with the z-axis perpendicular to the horizontal plates is fixed in the middle of the layer. As usually, viscous heating and volume viscosity effects can safely be neglected.

Realistic rigid boundary conditions are taken at the two boundaries for the velocity,

$$\vec{u} = 0 \text{ at } z = \pm\frac{d}{2} \tag{2.4}$$

and fixed values for the temperature

$$T = T_0 + \frac{\Delta T}{2} \text{ at } z = -\frac{d}{2}, \tag{2.5}$$

$$T = T_0 - \frac{\Delta T}{2} \text{ at } z = +\frac{d}{2}. \tag{2.6}$$

Here T_0 denotes the mean temperature $T_0 = (T_1 + T_2)/2$ and $\Delta T = (T_1 - T_2) > 0$ is the temperature difference across the layer.

We focus in this work on weakly non-Boussinesq convection, so we keep the temperature dependence of the various fluid properties to leading order, and expand them about the mean temperature T_0 (Busse (1967)),

$$\frac{\rho(T)}{\rho_0} = 1 - \gamma_0 \frac{T - T_0}{\Delta T}(1 + \gamma_1 \frac{T - T_0}{\Delta T}) + ... \tag{2.7}$$

$$\frac{\nu(T)}{\nu_0} = 1 + \gamma_2 \frac{T - T_0}{\Delta T} + ... \tag{2.8}$$

$$\frac{\lambda(T)}{\lambda_0} = 1 + \gamma_3 \frac{T - T_0}{\Delta T} + ... \tag{2.9}$$

$$\frac{c_p(T)}{c_{p0}} = 1 + \gamma_4 \frac{T - T_0}{\Delta T} + ... \tag{2.10}$$

Here ρ_0, ν_0, λ_0, and c_{p0} denote the values of the respective quantities at the mean temperature T_0. The dots denote higher-order terms to be neglected. We assume an experimental procedure in which T_0 is kept constant while the main control parameter ΔT is varied. The quantities $\gamma_i/\Delta T, i = 0, 2, 3, 4$, which describe, respectively, the slope of the density, viscosity, heat conductivity, and heat capacity at T_0, are then fixed as well. Thus, the γ_i represent the change of the respective fluid property across the fluid layer and are therefore linear in the main control parameter ΔT,

$$\gamma_i(T) = \gamma_i^c \left(1 + \frac{\Delta T - \Delta T_c}{\Delta T_c}\right), \tag{2.11}$$

where γ_i^c denotes the non-Boussinesq coefficients evaluated at the onset of convection, $T = T_c$. For instance, in terms of α_0, the usual heat expansion coefficient at $T = T_0$, the non-Boussinesq coefficient γ_0 is given by $\gamma_0 = \Delta T\, \alpha_0$. Beyond the Boussinesq approximation also the curvature of $\rho(T)$ at T_0, which is proportional to $\gamma_0\gamma_1/\Delta T^2$, comes into play.

To transform the governing equations and boundary conditions to dimensionless form, the following scales are selected: for length d, time d^2/κ_0, velocity κ_0/d, pressure $\rho_0\nu_0\kappa_0/d^2$, and temperature $\nu_0\kappa_0/\alpha_0 g d^3$. This gives rise to two dimensionless quantities: the Prandtl number $Pr = \nu_0/\kappa_0$, and the Rayleigh number $R = \alpha_0 \Delta T g d^3/\nu_0\kappa_0$. Finally, we write the equations in terms of the dimensionless momentum density $v_i = \rho d u_i/\rho_0\kappa_0$ instead of the velocities.

Since the fluid velocities are small compared to the sound velocity we make the anelastic approximation (Gough (1969)) and neglect the time derivative in the continuity equation (2.2). This simplifies the computation considerably since it reduces the number of evolution equations. Furthermore, v_i becomes a solenoidal field, which can be represented in

the standard poloidal-toroidal decomposition by two velocity potentials (Busse (1989)) automatically enforcing the mass conservation.

The conduction solution ($\vec{v} = 0$) of (2.3) with (2.5,2.6,2.7,2.9,2.10) is given by

$$T_{cond} = T_0 + R\left(-z - \frac{\gamma_3}{2}(z^2 - \frac{1}{4}) + \mathcal{O}(\gamma_3^2)\right). \tag{2.12}$$

We rewrite the temperature T in terms of the deviation Θ from the conductive profile neglecting its $\mathcal{O}(\gamma_3^2)$-contribution,

$$\Theta = T - T_{cond} = T - T_0 - R\left(-z - \frac{\gamma_3}{2}(z^2 - \frac{1}{4})\right). \tag{2.13}$$

We then obtain as the final dimensionless equations

$$\frac{1}{Pr}\left(\partial_t v_i + v_j\partial_j\left(\frac{v_i}{\rho}\right)\right) = -\partial_i p + \delta_{i3}\left(1 + \gamma_1(-2z + \frac{\Theta}{R})\right)\Theta + \\ +\partial_j\left[\nu\rho\left(\partial_i(\frac{v_j}{\rho}) + \partial_j(\frac{v_i}{\rho})\right)\right] \tag{2.14}$$

$$\partial_j v_j = 0, \tag{2.15}$$

$$\partial_t\Theta + \frac{v_j}{\rho}\partial_j\Theta = \frac{1}{\rho c_p}\partial_j(\lambda\partial_j\Theta) - \gamma_3\partial_z\Theta - R\frac{v_z}{\rho}(1 + \gamma_3 z). \tag{2.16}$$

The dimensionless boundary conditions are

$$\vec{v}(x, y, z, t) = \Theta(x, y, z, t) = 0 \text{ at } z = \pm\frac{1}{2}. \tag{2.17}$$

The nondimensionalized fluid parameters (2.7)-(2.10) read now:

$$\rho(\Theta) = 1 - \gamma_0(-z + \frac{\Theta}{R}), \tag{2.18}$$

$$\nu(\Theta) = 1 + \gamma_2(-z + \frac{\Theta}{R}), \tag{2.19}$$

$$\lambda(\Theta) = 1 + \gamma_3(-z + \frac{\Theta}{R}), \tag{2.20}$$

$$c_p(\Theta) = 1 + \gamma_4(-z + \frac{\Theta}{R}). \tag{2.21}$$

We consider the non-Boussinesq effects to be weak and keep in all material properties only the leading-order temperature dependence beyond the Boussinesq approximation. Therefore the γ_1-term appears explicitly in (2.14), while in all other terms it would constitute only a quadratic correction just like the terms omitted in (2.7)-(2.10). Correspondingly, we expand the denominators in (2.14,2.16) that contain material properties to leading order in the γ_i. In analogy to Busse (1967), we further omit non-Boussinesq terms that contain cubic nonlinearities in the amplitudes v_i or Θ, as they arise from the expansion of the advection terms $v_j\partial_j(v_i/\rho)$ and $(v_j/\rho)\partial_j\Theta$ when the temperature-dependence of the density is taken into account. Since we will be considering Rayleigh numbers up to twice the critical value, which implies enhanced non-Boussinesq effects, these approximations may lead to quantitative differences compared to the fully non-Boussinesq system, even though the temperature-dependence of the material properties themselves may quite well be described by a linear (or quadratic in the case of the density) approximation.

In the weakly nonlinear regime hexagon and roll patterns are described by the amplitudes A_i of the three dominant Fourier modes associated with the wavevectors $\mathbf{q_1} =$

$q(1,0)$, $\mathbf{q_2} = q/2(-1,\sqrt(3))$, $\mathbf{q_3} = q/2(-1,-\sqrt(3))$. Roll solutions correspond to $A_1 \neq 0$, $A_2 = A_3 = 0$ and hexagons to $A_1 = A_2 = A_3 \neq 0$, while for mixed hexagon solutions one has $A_1 \neq A_{2,3} \neq 0$. The amplitudes satisfy the well known coupled amplitude equations (e.g. Cross & Hohenberg (1993)),

$$\partial_t A_1 = \epsilon A_i - \delta \overline{A}_2 \overline{A}_3 - g_1 |A_1|^2 A_1 - g_2(|A_2|^2 + |A_3|^2)A_1. \tag{2.22}$$

The calculation of the coefficients δ, g_i involves vertical averages over certain products of the critical eigenvector components, which are obtained from a linearization of (2.14,2.16).

The quadratic coefficient δ arises from the NOB-effects. To leading order in the γ_i^c it has been calculated first by Busse (1967) and is proportional to Busse's parameter Q,

$$Q = \sum_{i=0}^{4} \gamma_i^c \mathcal{P}_i, \tag{2.23}$$

which is the conventional measure for the strength of the NOB-effects.† It characterizes the breaking of the up-down symmetry, which renders at most one of the two types of hexagons stable. For positive Q (gases) g-hexagons with down flow in the center are preferred (down-hexagons), whereas for negative Q (liquids) l-flow hexagons are observed, which are characterized by an up-welling in their center (up-hexagons). In Busse (1967) the cubic coefficients g_i are calculated for $\gamma_i^c = 0$, which is consistent with the assumption of small γ_i^c, $\gamma_i^c = \mathcal{O}(A_i)$. In the case of finite γ_i^c, as considered in our work, the calculation needs some refinement along the lines presented by Plaut & Pesch (1999).

The stability of weakly nonlinear roll and hexagon patterns is determined by a linear stability analysis of the various solutions of Eq. (2.22). The resulting stability diagram is sketched schematically in Fig.1 for the case $g_2 > g_1$. The hexagons arise unstably from the conductive state in a transcritical bifurcation and become stable through a saddle-node bifurcation. When the heating, i.e. ϵ, is increased they become unstable in a steady transcritical bifurcation involving a mixed-mode solution. The rolls in turn are unstable at threshold and become stable through a steady bifurcation when the control parameter is increased.

We focus in this paper on the stability properties of the patterns in the strongly nonlinear regime. They are determined by a Galerkin method (e.g. Busse & Clever (1979)). We use a Fourier expansion on a hexagonal lattice in the lateral directions. The Fourier wave vectors $\mathbf{q}$ are constructed as linear combinations of the hexagonal basis vectors $\mathbf{b}_1 = q(1,0)$ and $\mathbf{b}_2 = q(1/2,\sqrt{3}/2)$ as $\mathbf{q} = m\mathbf{b}_1 + n\mathbf{b}_2$ with the integers m and n in the range $|m\mathbf{b}_1 + n\mathbf{b}_2| \leq n_q q$. The largest wavenumber is then $n_q q$ and the number of Fourier modes retained is given by $1 + 6\sum_{j=1}^{n_q} j$. Typically we used $n_q = 3$. The top and bottom boundary conditions are satisfied by using appropriate combinations of trigonometric and Chandrasekhar functions in z (Chandrasekhar (1961); Busse (1967)). In most of the computations we used $n_z = 6$ modes for each field in Eq. (2.14,2.15,2.16). The linear analysis yields the critical Rayleigh number R_c as well as the critical wavenumber q_c. Both depend on the NOB-coefficients γ_i^c which in turn depend on R_c. Thus, in principle one obtains an implicit equation for the γ_i^c. The shift in the critical Rayleigh number away from the classical value $R_c = 1708$ due to the NOB-effects is, however, quite small (less than 1 percent) and therefore the resulting change in the γ_i^c is negligible. In this paper we therefore choose the γ_i^c corresponding to $R_c = 1708$.

To investigate the nonlinear hexagon solutions, we start with the standard weakly

† Note that Busse's calculation of $\mathcal{P}_3$ contained a small error (see Bodenschatz *et al.* (2000), p. 742, where $\mathcal{P}$ is used instead of Q.)

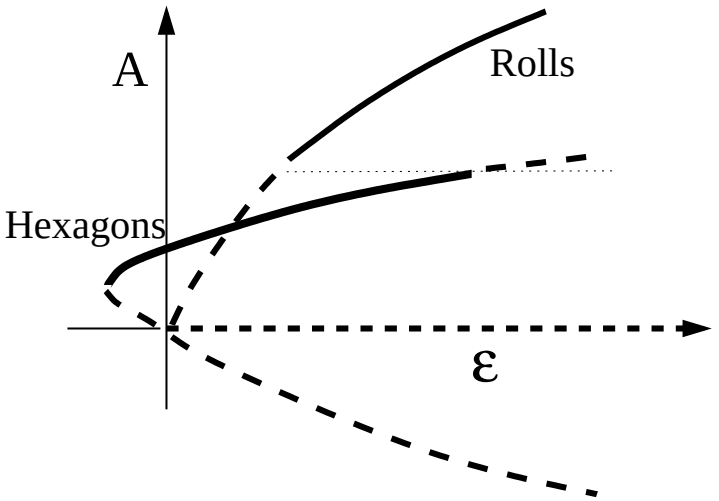

FIGURE 1. Sketch of the bifurcation diagram for hexagons and rolls in the weakly non-linear regime for NOB-convection. The continuous lines correspond to stable states and dashed lines to unstable ones. The dotted line represents the mixed modes.

nonlinear analysis to determine the coefficients of the three coupled amplitude equations for the modes making up the hexagonal pattern. To obtain the fully nonlinear solutions requires the solution of a set of nonlinear algebraic equations for the expansion coefficients with respect to the Galerkin modes. This is achieved with a Newton solver for which the weakly nonlinear solutions serve as convenient starting solutions. In the Galerkin code amplitude instabilities are tested by linear perturbations of the expansion coefficients. In addition, modulational instabilities have to be considered, which involves the introduction of Floquet multipliers $\exp(i\mathbf{s}\cdot(x,y))$ with $|\mathbf{s}| \ll q$.

We also study the temporal evolution of the system. For that we employ a Fourier spectral code on a rectangular grid that uses the same vertical modes as the Galerkin stability code. To solve for the time dependence we have chosen a fully implicit scheme for the linear terms, whereas the nonlinear parts are treated explicitly (second order Adams-Bashforth method). The time step is typically taken to be $t_v/500$, where t_v is the vertical diffusion time. We have tested that the stability regimes obtained from the Galerkin analysis are consistent with the direct numerical simulations.

3 Linear Stability of Hexagons

Instead of extensive parameter studies, we present in this work specific, interesting scenarios that should be experimentally realizable. We focus our investigation on water, which has a moderate Prandtl number and for which reentrant hexagons should be readily accessible in convection cells with conventional layer thickness d in a range of temperatures close to room temperature.

3.1 Amplitude instabilities

In our analysis, we first concentrate on spatially periodic solutions with the wavenumber fixed at the critical wavenumber and discuss their domains of existence and stability as a function of the control parameter $\epsilon = (R - R_c(\gamma_i^c))/R_c(\gamma_i^c)$. We have chosen three different cells with thickness $d = 1.5,\ 1.8,$ and $2.1\,mm$, respectively. The case $d = 1.8\,mm$ is of

T_0 [^oC]	ΔT_c [^oC]	Pr	γ_0^c	γ_1^c	γ_2^c	γ_3^c	γ_4^c	Q
20	20.63	6.93	0.0042	0.5693	-0.5186	0.0649	-0.0049	-4.612
25	15.16	6.10	0.0038	0.2952	-0.3370	0.0434	-0.0022	-2.489
28	12.94	5.68	0.0036	0.2122	-0.2725	0.0352	-0.0013	-1.837
32	10.74	5.18	0.0034	0.1440	-0.2126	0.0273	-0.0005	-1.292
36	9.12	4.76	0.0032	0.1023	-0.1709	0.0216	0.0001	-0.954
40	7.87	4.38	0.0030	0.0755	-0.1405	0.0173	0.0004	-0.731
50	5.75	3.62	0.0026	0.0400	-0.0926	0.0104	0.0007	-0.428
60	4.42	3.05	0.0023	0.0245	-0.0654	0.0064	0.0006	-0.287

TABLE 1. Values for the Prandtl number Pr, non-Boussinesq coefficients γ_i^c, and Busse's parameter Q for water at the onset of convection as a function of the mean temperature and the temperature difference. The liquid layer has a depth of $d = 1.8\,mm$.

particular interest since it has been studied in previous experiments (Pampaloni *et al.* (1992)).

Tab. 1 gives the non-Boussinesq coefficients and the Q-value at the onset of convection for a representative range of mean temperatures T_0 in a fluid layer of thickness $d = 1.8\,mm$†. As indicated before, the γ_i are linear in the temperature difference ΔT (see 2.11) and therefore they depend on ϵ,

$$\gamma_i = \gamma_i^c(1+\epsilon). \tag{3.1}$$

Note that with increasing mean temperature the critical temperature difference ΔT_c (given in the second column of Tab. 1) decreases. Therefore the variation of the fluid properties across the layer at the critical temperature and with it the coefficients γ_i^c also decrease with increasing temperature. Since we keep the mean temperature T_0 fixed when changing the Rayleigh number, the accessible range in ϵ is limited by the requirement that the temperature at the top plate, $T(z = d/2) = T_0 - \Delta T/2$, be above freezing. It turns out that the full range $0 \le \epsilon \le 1$ is then only accessible for average temperatures T_0 above a certain temperature T_0^f, which is 20^oC for $d = 1.8\,mm$.

Using the Galerkin method, we extend the weakly nonlinear result sketched in Fig.1 (Busse (1967)) to the strongly nonlinear regime. Fig.2 shows the resulting stability limits for hexagons and for rolls. As predicted by weakly nonlinear theory, the hexagons are linearly stable for very small ϵ. For not too small values of the mean temperature T_0 and and layer thickness d the hexagons become unstable as the control parameter is increased. For the convection cells investigated here, the hexagon patterns undergo then a second steady bifurcation as the control parameter is increased further and become stable again.

† These values were obtained with a code kindly provided by G. Ahlers.

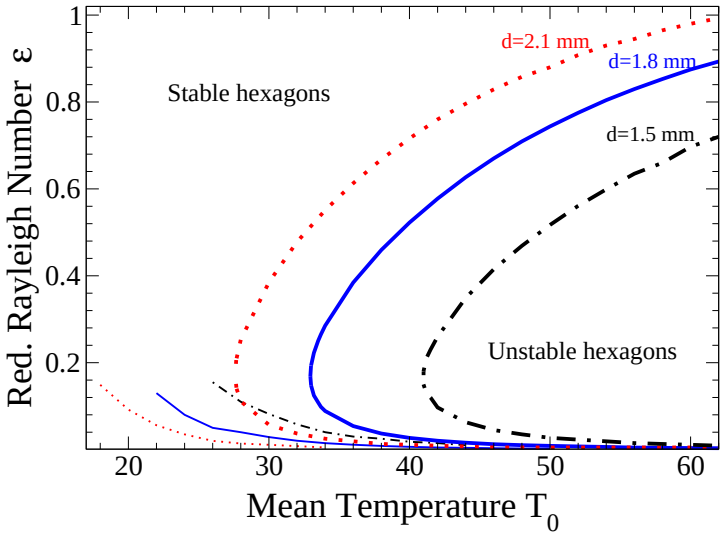

FIGURE 2. Stability regions for water with respect to amplitude perturbations for three fluid depths: $d = 2.1\,mm$ (dotted lines), $d = 1.8\,mm$ (full lines), $d = 1.5\,mm$ (dot-dashed line). Thick curves: stability boundaries for hexagons. Thin curves: stability boundaries for rolls. For a given depth, rolls are stable above the thin line, and hexagons unstable in the inner region of the thick line.

That is to say, the hexagons are reentrant. As the mean temperature is decreased or the layer thickness is decreased the critical heating and with it the non-Boussinesq effects increase. This shifts the point of reentrance to lower ϵ and the lower stability limit to higher ϵ, decreasing the ϵ-range over which the hexagons are unstable, until the two limits merge at a temperature T_m. For $T_0 < T_m$ the hexagons are amplitude-stable over the whole range of ϵ considered ($0 \leq \epsilon \leq 1$).

Reentrant hexagons have been observed by Roy and Steinberg (Roy & Steinberg (2002)) in SF_6 near the thermodynamical critical point. In that work the origin of reentrance is attributed to the large compressibility of the fluid in this parameter regime. By assuming that the working fluid is incompressible, which is an excellent approximation for water, our computations show that high compressibility is not needed for reentrance.

We have also computed the stability of rolls with respect to amplitude perturbations. The corresponding stability limits are indicated in Fig.2 by thin lines.They cannot be extended below the values of T_0 shown in Fig.2 since then the liquid would freeze at the top plate. Thus the regime $T_0 < T_0^f$ is not accessible in experiments. Below the thin curves rolls are unstable, but they become linearly stable when increasing ϵ beyond the lines. As the non-Boussinesq effects become stronger the stabilization of rolls is shifted to larger ϵ. In contrast to the hexagons, for the convection cells investigated here the rolls do not undergo a second bifurcation, which would destabilize them, and remain amplitude-stable up to the largest values of ϵ considered. For strong non-Boussinesq effects one has therefore a very large range of parameters over which the competing rolls and hexagons are both linearly amplitude-stable.

The amplitude-stability limits of the hexagons and rolls depend, of course, on their wavenumber. This is illustrated in Fig. 3, where we fix a mean temperature T_0 and determine the stability limits of the hexagons as a function of their wavenumber q. Interestingly, for $T_0 = 36\,^oC$ (Fig.3(a)) the hexagons become more stable for small and for

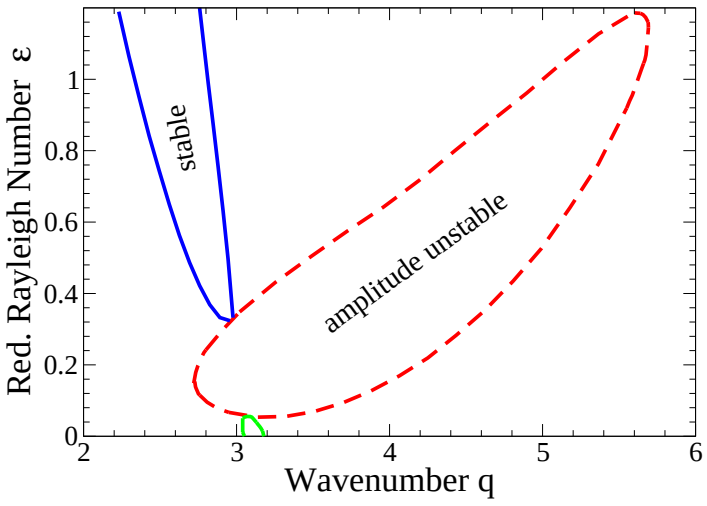

(a)

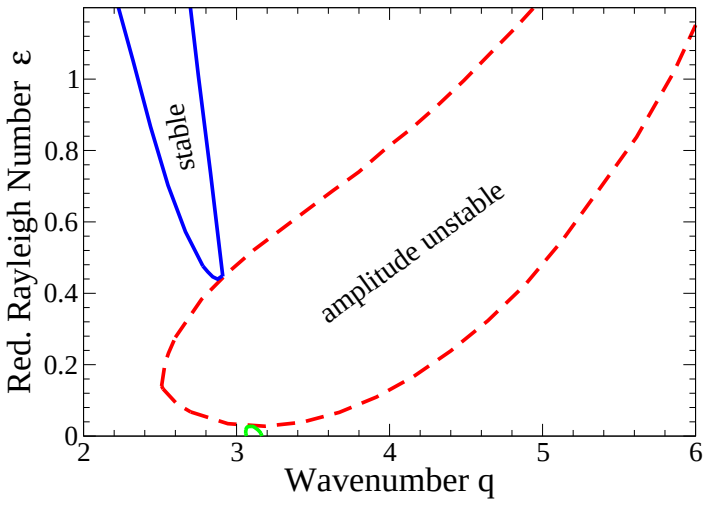

(b)

FIGURE 3. Stability regions for hexagons in water with respect to amplitude (dashed line) and side-band perturbations (solid line). The depth of the fluid layer is $d = 1.8\,mm$. Figure (a) $T_0 = 36\,^oC$, (b) $T_0 = 40\,^oC$. Hexagons are stable with respect to amplitude perturbations outside the dashed-line region, and stable with respect to side-band perturbation inside the solid-line region.

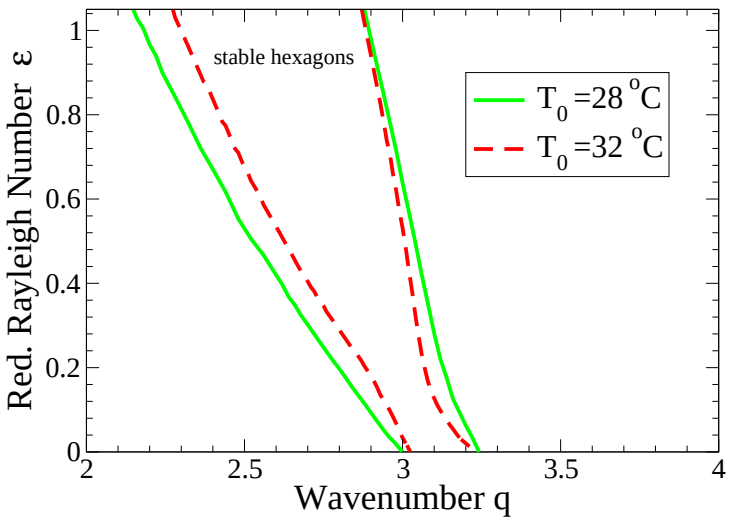

FIGURE 4. Stability regions for water with respect to side-band perturbations. The fluid depth is $d = 1.8\,mm$. Solid line: $T_0 = 28^oC$. Dashed line: $T_0 = 32^oC$.

large wavenumbers and the instability region forms a bubble-like, closed curve, outside of which the hexagons are stable with respect to amplitude perturbations. These bubbles are 'hyper-surfaces' in $q - \epsilon - T_0$-space. With decreasing non-Boussinesq effects (increasing T_0) the bubble grows and extends to larger values of ϵ. Eventually, the upper part of the bubble is shifted to ϵ-values beyond the range considered in this paper (Fig.3(b) for $T_0 = 40^oC$).

3.2 Side-Band Perturbations

Using the Galerkin method, we have studied the stability of the hexagons with respect to long- and short-wave perturbations as shown in Fig.3. We find that over the whole range $0 \leq \epsilon \leq 1$ the only relevant side-band perturbations are long-wave and steady, as it is the case in the weakly nonlinear regime. The long-wave perturbations involve longitudinal and transverse phase modes, which can be described by two coupled evolution equations (Lauzeral *et al.* (1993); Hoyle (1995); Echebarria & Pérez-García (1998)). The stability limits obtained from the Galerkin analysis are shown in Fig. 3. In this parameter regime the stability region consists of two disconnected domains, reflecting the reentrant nature of the hexagons. The stability domain near onset is very small and closes up as the amplitude stability limit is reached. This behavior corresponds to that from the coupled Ginzburg-Landau equations (2.22) (Lauzeral *et al.* (1993)). In the reentrant regime the stable domain opens up again in an analogous fashion when the amplitude-stability limit is surpassed. Note that the stability boundaries are leaning toward lower wavenumbers. Thus, stable reentrant hexagonal patterns are expected to have wavenumbers below q_c.

As the mean temperature is lowered the bubble of the amplitude instability shrinks and eventually the bubble disappears (Fig.4). The side-band stability limit reaches then without interruption from the strongly nonlinear regime all the way down to threshold (more precisely to the saddle-node bifurcation of the hexagons). As the non-Boussinesq effects become yet stronger the range of stable wavenumbers widens.

4 Origin of Reentrant Hexagons

At first the appearance of stable reentrant non-Boussinesq hexagons seems quite surprising, in particular, considering the relatively small values of ϵ for which the restabilization of the hexagons can occur. We have identified two major factors that contribute to their appearance: the ϵ-dependence of the non-Boussinesq coefficients and the existence of stable hexagons at large Rayleigh numbers already in the Boussinesq case (Assenheimer & Steinberg (1996); Clever & Busse (1996); Busse *et al.* (1999)).

As indicated earlier (cf. (3.1)), the non-Boussinesq coefficients γ_i increase linearly with the temperature difference, $\gamma_i = \gamma_i^c \cdot (1+\epsilon)$. For the weakly nonlinear description in terms of the three amplitudes A_i that make up the hexagon pattern this implies that the coefficient of the resonance-triad term coupling the three amplitudes at quadratic order grows with ϵ. As a consequence, to $\mathcal{O}(\epsilon^2)$ with $A = \mathcal{O}(\epsilon^{1/2})$ one obtains the following equations

$$\begin{aligned}\partial_t A_1 = {} & \xi^2(\mathbf{n}_i\cdot\nabla)^2 A_i + \epsilon A_i - (\delta+\mu\epsilon)\overline{A}_2\overline{A}_3 - g_1\,|A_1|^2 A_1 \\ & -g_2(|A_2|^2+|A_3|^2)A_1 + \overline{A}_2\overline{A}_3\left(g_3|A_1|^2 + g_4(|A_2|^2+|A_3|^2)\right)\big) \\ & +g_5 A_1(A_1A_2A_3) + g_6 A_1(\overline{A}_1\overline{A}_2\overline{A}_3),\end{aligned} \tag{4.1}$$

where $\mathbf{n}_i = \mathbf{q}_i/|\mathbf{q}_i|$ and the coefficient μ expresses the ϵ-dependence of the γ_i. The gradient term allows long-wave modulations of the amplitude to capture side-band instabilities. For simplicity, we have omitted nonlinear gradient terms like $\overline{A}_2(\mathbf{n}_3\cdot\nabla)A_3$ etc. (Echebarria & Pérez-García (1998); Nuz *et al.* (1998)). Note that a correction linear in ϵ of the quadratic resonance term has been considered previously in the context of hexagonal patterns in ferrofluids exposed to a magnetic field (Friedrichs & Engel (2001)). If the terms quartic in the amplitudes are neglected the stability analysis of hexagons with respect to rolls is quite simple and yields at the critical wavenumber q_c the stability limits

$$\epsilon_\pm = \frac{a}{\mu^2}\left[1 - \frac{\mu\delta}{a} \pm \sqrt{1-2\frac{\mu\delta}{a}}\right], \qquad a = \frac{(g_1-g_2)^2}{2(2g_1+g_2)}. \tag{4.2}$$

Thus, the strengthening of the resonant-triad interaction with ϵ can lead to a second change of stability of the hexagons, which stabilizes them. For weak ϵ-dependence, i.e. $\mu\delta \ll a$, the restabilization occurs at large values of ϵ,

$$\epsilon_+ = \frac{(g_1-g_2)^2}{2g_1+g_2}\mu^{-2} + \mathcal{O}(\mu^{-1}). \tag{4.3}$$

With increasing μ, however, the restabilization is shifted to ever lower values of ϵ and for $\mu = \mu_M \equiv a/(2\delta)$ both bifurcations merge. For $\mu > \mu_M$ the hexagons do not exhibit any instability to rolls. The stability limits of rolls are given by an expression analogous to that for $\epsilon_\pm$ in (4.2) with a given by $a = (g_1-g_2)^2/2g_1$.

Strictly speaking, the terms that are quartic in the amplitudes also contribute to the restabilization. While the sign of μ is known to be positive due to the known increase of the non-Boussinesq coefficients with ϵ, one cannot make a general statement about the sign or magnitude of the quartic coefficients g_3, g_4, g_5, g_6. Thus, even for a qualitative prediction regarding the occurrence of the reentrance based on the amplitude-equation model (4.1) one would have to derive the amplitude equation from the Navier-Stokes equations to quartic order. This is beyond the scope of the present paper. Furthermore, since for the parameter range considered in this paper the reentrance occurs at a finite value of ϵ the quartic terms do not merely constitute small corrections and it is, a priori,

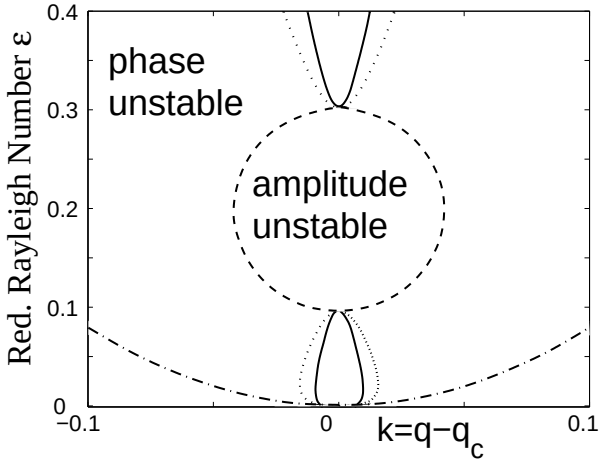

FIGURE 5. Amplitude and side-band stability limits based on the extended Ginzburg-Landau-equation model (4.1) with $\xi = 1$, $g_3 = g_4 = g_5 = g_6 = 0$. Shown are the neutral curve (dashed-dotted), the long-wave side-band stability limit (solid and dotted), and the amplitude stability limit (dashed). Hexagons are stable inside the solid lines.

not clear how reliable the extended amplitude equations (4.1) are. If the reentrance occurred in the immediate vicinity of threshold it could be captured rigorously within the amplitude equations in the distinguished limit $g_1 - g_2 = \mathcal{O}(\epsilon^{1/2})$, in which case ϵ_+ would be small. Even without going into details of such an asymptotic analysis it becomes clear, however, that the growth of the γ_i with ϵ has the potential to induce the reentrance of stable hexagons.

Given the discussion above, we consider (4.1) as a simple qualitative model that may capture certain features of the reentrant hexagons. We show in Fig.5 the side-band stability limits obtained from this model in a typical case. Each of the two long-wave phase modes of hexagons can lead to an instability. For the intermediate Prandtl numbers considered here mean flows are not important and the transverse phase mode (solid line in Fig.5) determines the stability limit except for an extremely small range in ϵ near threshold. For strong mean flows the longitudinal phase mode (dotted line) can dominate the transverse mode (Young & Riecke (2002); Semwogerere & Schatz (2003)). In qualitative agreement with the full numerical result (cf. Fig.3), the model (4.1) yields a side-band stable range for the reentrant hexagons that closes as the amplitude instability is approached with decreasing ϵ. Since we have not included any nonlinear gradient terms (cf. Echebarria & Pérez-García (1998)) the stability limits are strictly symmetric, in contrast to the full numerical results.

The second factor that contributes to the occurrence of reentrant non-Boussinesq hexagons is the fact that even in the Boussinesq case hexagons can be stable for large Rayleigh numbers (above $\epsilon \approx 1$), as first observed in convection experiments close to the thermodynamical critical point of SF_6 (Assenheimer & Steinberg (1996)). A subsequent numerical stability analysis confirmed the existence of such stable OB-hexagons and attributed their appearance to the formation of plumes (Clever & Busse (1996); Busse *et al.* (1999)).

Fig.6 provides a quantitative assessment of the impact of these two mechanisms. Above the dashed-dotted line hexagons with wavenumber q_c become amplitude-stable in the

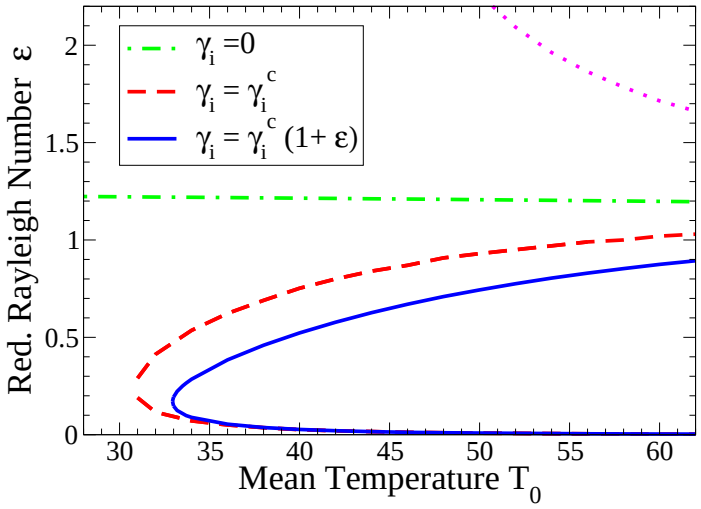

FIGURE 6. Stability regions for hexagons with respect to amplitude perturbations in water for $d = 1.8\,mm$. Solid line: stability limit when the dependence of γ on the temperature is taken into account, $\gamma_i = \gamma_i^c(1+\epsilon)$. Dashed line: stability limit when the γ_i are fixed to their critical value, $\gamma_i = \gamma_i^c$. OB-hexagons are stable above the dashed-dotted line, $\gamma_i = 0$. Down-hexagons are stable above the dotted line for $\gamma_i = \gamma_i^c(1+\epsilon)$.

Boussinesq case $\gamma_i = 0$. The very slight dependence of the stability limit on the mean temperature is due to the variation of the Prandtl number with T_0, which decreases from $Pr = 5.4$ at $T_0 = 30\,^oC$ to $P = 3.0$ at $T_0 = 60\,^oC$. With the non-Boussinesq effects included, the stabilization of the hexagons occurs at lower values of the control parameter. When the γ_i are kept independent of ϵ, $\gamma_i = \gamma_i^c$, the change in the stability becomes significant mostly for small T_0 where the non-Boussinesq effects are already large at onset as characterized by Busse's Q value, which reaches $Q = -1.5$ at $T_0 = 30\,^oC$ (cf. Table 1). When the ϵ-dependence of the γ_i is included, $\gamma_i = \gamma_i^c(1+\epsilon)$, large changes in stability are found even for high T_0, where the non-Boussinesq effects are quite weak at onset ($Q = -0.3$ at $T_0 = 60\,^oC$). Thus, while the ϵ-dependence is not necessary for reentrance it has a substantial quantitative effect on it.

Since in the Boussinesq-case up- and down-hexagons are equivalent and become stable simultaneously it is to be expected that for weak non-Boussinesq effects both types of hexagons can become stable for large Rayleigh numbers, with the stabilization occurring, however, at different values of the Rayleigh number. For the up-hexagons this stabilization corresponds to a reentrance. The stabilization of the down-hexagons is indicated in Fig.6 by a dotted line. As the non-Boussinesq effects become stronger the down-hexagons require ever higher Rayleigh numbers for stabilization.

5 Numerical Simulations

To make closer contact with what experimental investigations would be expected to find we perform also direct numerical simulations of (2.14,2.16). The most important experimental aspects that are not captured by our Galerkin stability analysis are the

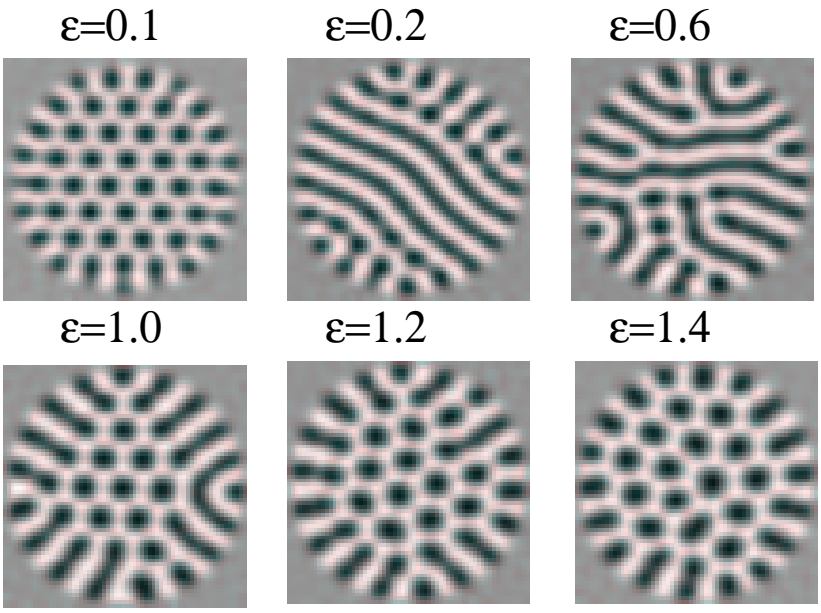

FIGURE 7. Succession of snapshots for $T_0 = 24\,^oC$ in a circular cell of water of thickness $d = 1.8\,mm$. The diameter of the cell is $L = 8 \cdot 2\pi/q$.

lateral boundary conditions. To mimic the circular containers that are typically used in experiments we apply a strong radial subcritical ramp in the Rayleigh number that suppresses any convection outside a certain radius (cf. Decker *et al.* (1994), Fig.1 in Bodenschatz *et al.* (2000)).

Snapshots of a circular cell with diameter $L = 8 \cdot 2\,\pi/q$ and layer thickness $d = 1.8\,mm$ are shown in Fig.7. For the mean temperature considered, $T_0 = 24\,^oC$, both rolls and hexagons are stable with respect to amplitude perturbations for $\epsilon \geq 0.1$ (cf. Fig.2). In a variational system one would then expect that after starting from random initial conditions the system would evolve toward the state with minimal energy. In general, the Navier-Stokes equations (2.14,2.16) and their weakly nonlinear description (4.1) are not variational. However, if among the quartic terms in (4.1) only the term involving μ is retained the amplitude equations are variational and one can show that hexagons have lower energy close to threshold and in the case of reentrance also for large values of ϵ. In the intermediate ϵ-range rolls may have lower or higher energy, depending on the parameters.

In the non-variational case the relevant criterion determining the final state is whether domains of hexagons invade domains of rolls or vice versa. We have not made a detailed study of the propagation of such invading fronts, but on a qualitative level the simulations presented in Fig.7 fit readily into this framework. Near threshold ($\epsilon = 0.1$) the cell is completely filled with regular hexagons, except for a narrow ring of roll-like structures that are driven by the boundaries. When the heating is increased ($\epsilon = 0.2$) rolls become linearly stable and the rolls that are driven by the boundary invade most of the cell. With increasing ϵ the roll pattern becomes more irregular, exhibiting various orientations and interspersed defects ($\epsilon = 0.6$). So far the scenario is very similar to that observed in experiments by Pampaloni *et al.* (1992) for $T_0 = 28^oC$ (see also Fig.8 below). While the roll pattern persists near the boundaries for yet larger values of ϵ, a domain of ordered hexagons appears in the center of the cell for $\epsilon = \mathcal{O}(1)$. The size of the inner domain of

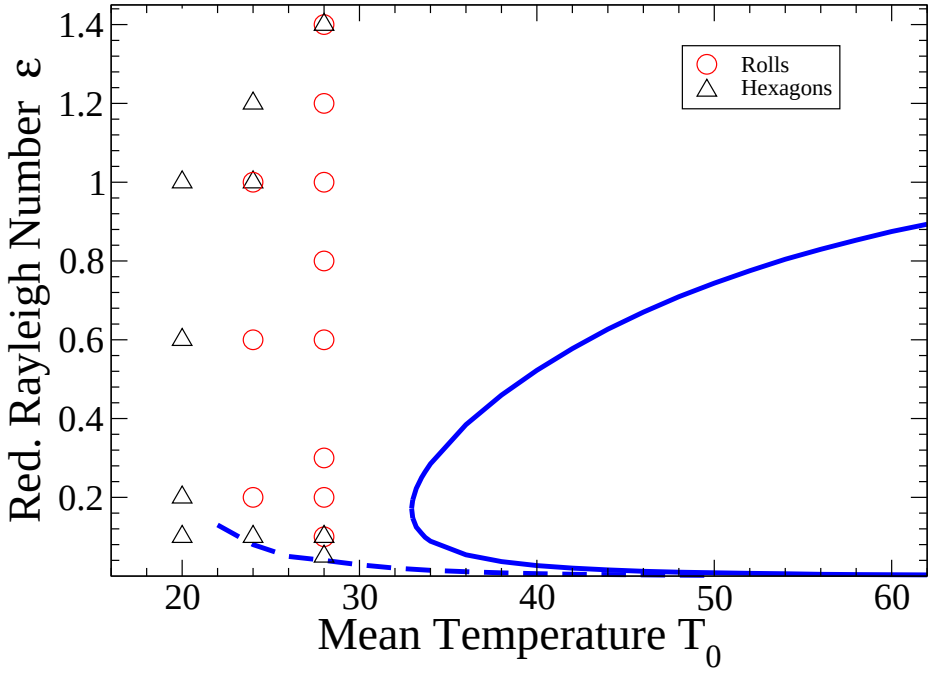

FIGURE 8. Results of simulations for a circular cell of thickness $d = 1.8\,mm$ and diameter $L = 8 \cdot 2\,\pi/q$. The simulations have been carried out for $T_0 = 20\,^oC$, $24\,^oC$, $28\,^oC$. Circles correspond to rolls and triangles to hexagons. The stability limits for amplitude instabilities are also shown for hexagons (full line) and for rolls (dashed line).

hexagons grows with increasing ϵ and for $\epsilon = 1.4$ the hexagons fill essentially the whole convection cell. The growing of the hexagon domain can be understood to arise from a balance between the increasing tendency of the hexagon domains to invade domains with roll convection on the one hand and the predominance of roll convection near the boundaries on the other hand.

A comparison of the snapshot at $\epsilon = 0.1$ with that at $\epsilon = 1.4$ shows that the reentrant hexagons arising from random initial conditions have a smaller wavenumber than the hexagons that appear at threshold. This trend is consistent with the results of the side-band stability calculations (Figs. 3, 4), which show that with increasing ϵ the wavenumber range of stable hexagons moves toward lower wavenumbers.

In Fig.8 the results of a set of simulations for three mean temperatures, $T_0 = 20\,^oC$, $T_0 = 24\,^oC$, and $T_0 = 28\,^oC$, are summarized. The circular cell has the same dimensions as before and again random initial conditions are used. The triangles denote parameter values for which the final state consists mostly of regular hexagons, while the circles indicate a final roll state. When both patterns coexist over the course of the simulation ($t_{max} = 200$) both symbols are drawn. The simulations show that for $T_0 = 20\,^oC$ the NOB-effects are so strong that hexagons are preferred over rolls over the full range of ϵ studied. As seen before in Fig.7, for a mean temperature of $T_0 = 24\,^oC$ an intermediate range of ϵ arises in which the final state consists of rolls. For $\epsilon = 1.0$ rolls and hexagons

coexist and for yet larger ϵ reentrant hexagons appear. If the mean temperature is increased further to $T_0 = 28\,^oC$ the same sequence: hexagons $\rightarrow$ rolls and hexagons $\rightarrow$ rolls $\rightarrow$ rolls and hexagons $\rightarrow$ hexagons is obtained. The only difference to the case $T_0 = 24^oC$ is that the reentrance is shifted to larger values of ϵ. It is worth noting that according to our computations Pampaloni *et al.* (1992) should have obtained stable reentrant hexagons if they had gone to larger values of the Rayleigh number. Fig.8 suggests that the transition lines between the different regimes follow the same trend as the stability limit for amplitude perturbations for the hexagons (solid line).

6 Conclusions

In this paper we have studied non-Boussinesq convection in water for realistic parameters and boundary conditions. We have complemented numerical stability analyses for periodic boundary conditions with direct numerical simulations that mimic set-ups used in usual laboratory experiments. Our main result is the finding of *reentrant* hexagons under sufficiently strong NOB-conditions, i.e. we find that the hexagon patterns, which typically become unstable to rolls not too far from threshold (Busse (1967)), can regain stability further above threshold. For strong, but realistic NOB-effects hexagons that become unstable at $\epsilon = 0.15$ can become stable again already at $\epsilon = 0.2$. For yet stronger NOB-effects hexagons are amplitude-stable over the whole range of ϵ investigated ($\epsilon < 1.5$). This stabilization over the whole range of ϵ is not due to a shifting of the initial transition from hexagons to rolls to ever increasing ϵ, but rather it is the result of a merging of the latter stability line with the line of restabilization.

Reentrant hexagons have been observed in experiments using SF_6 near its thermodynamic critical point as a working fluid (Roy & Steinberg (2002)). There the restabilization has been attributed to the strong compressibility in this regime. Our computations, being based on water as the working fluid, show that compressibility is not necessary for this phenomenon. We show that the reentrance is instead connected with the fact that even in the Boussinesq-case hexagons can become stable for sufficiently large ϵ, as has been observed experimentally (Assenheimer & Steinberg (1996)) and subsequently confirmed by stability computations (Busse *et al.* (1999); Clever & Busse (1996)). In the Boussinesq case two types of hexagons can coexist, up-hexagons characterized by an up-welling in their center (up-hexagons) and down-hexagons (Busse (1967)). The NOB-effects shift the stability limit of the up-hexagons to lower values of ϵ. This effect is strongly enhanced by the dependence of the NOB-effects on ϵ. A simple amplitude-equation model capturing this effect provides qualitative insight into the stability of the hexagons, including their side-band instabilities.

The connection between the reentrant hexagons and the Boussinesq hexagons suggests that even in the non-Boussinesq case down-hexagons may become linearly amplitude-stable, albeit for yet higher Rayleigh numbers. We show that this is indeed the case. We have not investigated their side-band instabilities and it is not clear whether they can coexist with up-hexagons or whether the domains of up-hexagons always invade domains of down-hexagons.

To address the stability and dynamics of the hexagon patterns in large-aspect ratio systems with non-periodic boundary conditions we have also performed direct numerical simulations of the Navier-Stokes equations. By a suitable strong variation of the local Rayleigh number we have implemented a qualitatively convincing model of a circular container (Decker *et al.* (1994)). For intermediate NOB-effects we confirm the experimentally observed scenario in the low-ϵ regime (Pampaloni *et al.* (1992)). Our computations suggest that even in this experimental set-up reentrant hexagons should have been accessible

experimentally for somewhat stronger heating ($\epsilon \approx 1.5$). For not much smaller mean temperature, i.e somwehat larger NOB-effects, we find that already for $\epsilon = 1$ the reentrant hexagons invade roll patterns and therefore persist even in the presence of side-walls. As expected based on the side-band stability calculations, the reentrant hexagons have a smaller wavenumber than the hexagons near onset.

Since in experiments the side walls always induce roll convection the transition between rolls and hexagons occurs when the velocity of a front separating the two states changes sign and not at the stability limit of the hexagons. It is therefore not possible to study the amplitude-stability limit of the hexagons in such cells. We expect, however, that by forcing hexagonal patterns near the walls either by an appropriate space-dependent heating (Semwogerere & Schatz (2002)) or by a suitably corrugated bottom plate (Bodenschatz (unpublished)) hexagons can be stabilized near the walls and the bulk stability of hexagons with respect to rolls can be investigated.

All of the present computations were performed for water as a working fluid, which has a relatively large Prandtl number. Large-scale mean flows are therefore not expected to be important. Within a Ginzburg-Landau model it was found previously that the side-band instabilities of hexagons can be modified for sufficiently strong mean-flows. In particular, the transverse long-wave instability can be replaced by a longitudinal long-wave instability (Young & Riecke (2002)). An interesting question is whether with realistic fluids this regime can be reached (e.g. in H_2Xe-mixtures Prandtl numbers as low as $Pr = 0.2$ (Liu & Ahlers (1997)) can be obtained).

The merging of the lower stability limit of hexagons with the restabilization line provides also an explanation for the large contiguous stability range that was found in rotating non-Boussinesq convection using water (Young *et al.* (2003)). An interesting question is how the restabilization interacts with the Hopf bifurcation of the hexagons to oscillating hexagons, which is induced by rotation (Swift (1984); Soward (1985); Echebarria & Riecke (2000); Madruga & Perez-Garcia (2004)).

We thank G. Ahlers for providing us with the code to determine the non-Boussinesq coefficient. We gratefully acknowledge support by the office of Basic Energy Sciences at the Department of Energy (DE-FG02-92ER14303).

REFERENCES

Assenheimer, M. & Steinberg, V. 1996 Observation of coexisting upflow and downflow hexagons in Boussinesq Rayleigh-Bénard convection. *Phys. Rev. Lett.* **76**, 756–759.

Bodenschatz, E. unpublished .

Bodenschatz, E., Cannell, D., DeBruyn, J. R., Ecke, R., Hu, Y., Lerman, K. & Ahlers, G. 1992 Experiments on 3 systems with nonvariational aspects. *Physica D* **61**, 77.

Bodenschatz, E., deBruyn, J. R., Ahlers, G. & Cannell, D. 1991 Transitions between patterns in thermal convection. *Phys. Rev. Lett.* **67**, 3078.

Bodenschatz, E., Pesch, W. & Ahlers, G. 2000 Recent developments in Rayleigh-Bénard convection. *Ann. Rev. Fluid Mech.* **32**, 709–778.

Busse, F. H. 1967 The stability of finite amplitude cellular convection and its relation to an extremum principle. *J. Fluid Mech.* **30**, 625.

Busse, F. H. 1989 Fundamentals of thermal convection. In *Mantle Convection: Plate Tectonics and Global Dynamics* (ed. W. Peltier), p. 23. Gordon and Breach (Montreux).

Busse, F. H. & Clever, R. M. 1979 Instabilities of convection rolls in a fluid of moderate prandtl number. *J. Fluid Mech.* **91**, 319.

Busse, F. H. & Clever, R. M. 1999 New patterns in Rayleigh-Bénard convection. In *Des Phénomènes Critiques au Chaos* (ed. P. Manneville), pp. 79–92. Saclay: DRECAM/SPEC CEA.

Busse, F. H., Clever, R. M. & Grote, E. 1999 Weakly nonlinear and fully nonlinear pattern formation in isotropic convection layers. *Chaos Solitons Fractals* **10** (4-5), 753–760.

Chandrasekhar, S. 1961 *Hydrodynamic and Hydromagnetic Stability*. Oxford: Clarendon.

Chiam, K.-H., Paul, M. R., Cross, M. C. & Greenside, H. S. 2003 Mean flow and spiral defect chaos in Rayleigh-Bénard convection. *Phys. Rev. E* **67**, 056206.

Clever, R. M. & Busse, F. H. 1996 Hexagonal convection cells under conditions of vertical symmetry. *Phys. Rev. E* **53**, R2037–R2040.

Cross, M. & Hohenberg, P. 1993 Pattern formation outside of equilibrium. *Rev. Mod. Phys.* **65**, 851.

Dangelmayr, G. 1986 Steady-state mode interactions in the presence of O(2)-symmetry. *Dyn. Stab. Systems* **1**, 159.

Davis, S. H. & Segel, L. A. 1968 Effects of surface curvature and property variation on cellular convection. *Phys. Fluids* **11** (3), 470.

Decker, W., Pesch, W. & Weber, A. 1994 Spiral defect chaos in Rayleigh-Bénard convection. *Phys. Rev. Lett.* **73**, 648.

Dubois, M., Bergé, P. & Wesfreid, J. 1978 Non-Boussinesq convective structure in water near 4-degrees-c. *J. Physique* **39**, 1253–1257.

Echebarria, B. & Pérez-García, C. 1998 Phase instabilities in hexagonal patterns. *Europhys. Lett.* **43**, 35.

Echebarria, B. & Riecke, H. 2000 Defect chaos of oscillating hexagons in rotating convection. *Phys. Rev. Lett.* **84**, 4838.

Egolf, D. A., Melnikov, I. V., Pesch, W. & Ecke, R. E. 2000 Mechanisms of extensive spatiotemporal chaos in Rayleigh-Bénard convection. *Nature* **404**, 733–736.

Friedrichs, R. & Engel, A. 2001 Pattern and wave number selection in magnetic fluids. *Phys. Rev. E* **6402**, 021406.

Gough, D. O. 1969 The anelastic approximation in thermal convection. *J. Atmos. Sci.* **26**, 448.

Hoyle, R. 1995 Nonlinear phase diffusion equations for the long-wave instabilities of hexagons. *Appl. Math. Lett.* **8** (3), 81.

Hu, Y., Ecke, R. & Ahlers, G. 1995 Time and length scales in rotating Rayleigh-Bénard convection. *Phys. Rev. Lett.* **74**, 5040.

Hu, Y., Pesch, W., Ahlers, G. & Ecke, R. E. 1998 Convection under rotation for Prandtl numbers near one: Küppers-Lortz instability. *Phys. Rev. E* **58**, 5821.

Küppers, G. & Lortz, D. 1969 Transition from laminar convection to thermal turbulence in a rotating fluid layer. *J. Fluid Mech.* **35**, 609.

Lauzeral, J., Metens, S. & Walgraef, D. 1993 On the phase dynamics of hexagonal patterns. *Europhys. Lett.* **24**, 707.

Liu, J. & Ahlers, G. 1997 Rayleigh-Bénard convection in binary-gas mixtures: Thermophysical properties and the onset of convection. *Phys. Rev. E* **55**, 6950–6968.

Madruga, S. & Perez-Garcia, C. 2004 Hexagonal patterns in a model for rotating convection. *Int. J. Bifurcation Chaos* **14**, 107–117.

Manogg, G. & Metzener, P. 1994 Strong resonance in 2-dimensional non-Boussinesq convection. *Phys. Fluids* **6**, 2944–2955.

Matley, R. G., Wong, W. Y., Thurlow, M. S., Lucas, P. G., Lees, M. J., Griffiths, O. J. & Woodcraft, A. L. 2001 Flow pattern dynamics in convecting liquid helium. *Phys. Rev. E* **63**, 045301.

Morris, S. W., Bodenschatz, E., Cannell, D. & Ahlers, G. 1993 Spiral defect chaos in large aspect ratio Rayleigh-Bénard convection. *Phys. Rev. Lett.* **71**, 2026.

Morris, S. W., Bodenschatz, E., Cannell, D. S. & Ahlers, G. 1996 The spatio-temporal structure of spiral-defect chaos. *Physica D* **97**, 164.

Nuz, A. E., Nepomnyashchy, A. A. & Pismen, L. M. 1998 Stability of non-equilateral hexagonal patterns governed by generalized amplitude equations. *Physica A* **249** (1-4), 179–183.

Palm, E. 1960 On the tendency towards hexagonal cells in steady convection. *J. Fluid Mech.* **8**, 183–192.

Palm, E., Ellingsen, T. & Gjevik, B. 1967 On occurrence of cellular motion in Bénard convection. *J. Fluid Mech.* **30**, 651.

Pampaloni, E., Pérez-Garía, C., Albavetti, L. & Ciliberto, S. 1992 Transition from

hexagons to rolls in convection in fluids under non-Boussinesq conditions. *J. Fluid Mech.* **234**, 393–416.

Plaut, E. & Pesch, W. 1999 Extended weakly nonlinear theory of planar nematic convection. *Phys. Rev. E* **59**, 1747–1769.

Prat, J., Mercader, I. & Knobloch, E. 2002 The 1 : 2 mode interaction in Rayleigh-Bénard convection with and without Boussinesq symmetry. *Int. J. Bifurcation Chaos* **12**, 281–308.

Proctor, M. & Jones, C. 1988 The interaction of two spatially resonant patterns in thermal convection. part 1. exact 1:2 resonance. *J. Fluid Mech.* **188**, 301–335.

Proctor, M. R. & Matthews, P. C. 1996 $\sqrt{2}$: 1 resonance in non-Boussinesq convection. *Physica D* **97**, 229.

Richter, F. M. 1978 Experiments on the stability of convection rolls in fluids whose viscosity depends on temperature. *J. Fluid Mech.* **89**, 553.

Roy, A. & Steinberg, V. 2002 Reentrant hexagons in non-Boussinesq Rayleigh-Bénard convection: Effect of compressibility. *Phys. Rev. Lett.* **88**, 244503.

Segel, L. A. 1965 Non-linear interaction of finite number of disturbances to a layer of fluid heated from below. *J. Fluid Mech.* **21**, 359.

Segel, L. A. & Stuart, J. T. 1962 On the question of the preferred mode in cellular thermal convection. *J. Fluid Mech.* **13**, 289–306.

Semwogerere, D. & Schatz, M. F. 2002 Evolution of hexagonal patterns from controlled initial conditions in a Bénard convection experiment. *Phys. Rev. Lett.* **88**, 054501.

Semwogerere, D. & Schatz, M. F. 2003 Secondary instabilities of hexagon patterns in a Bénard-Marangoni convection experiment. *preprint* .

Somerscales, E. F. & Dougherty, T. S. 1970 Observed flow patterns at initiation of convection in a horizontal liquid layer heated from below. *J. Fluid Mech.* **42**, 755.

Soward, A. M. 1985 Bifurcation and stability of finite amplitude convection in a rotating layer. *Physica D* **14**, 227–241.

Swift, J. W. 1984 Convection in a rotating fluid layer. In *Contemporary Mathematics Vol. 28*, p. 435. Providence: American Mathematical Society.

Walden, R. W. & Ahlers, G. 1981 Non-Boussinesq and penetrative convection in a cylindrical cell. *J. Fluid Mech.* **109**, 89–114.

Young, Y.-N. & Riecke, H. 2002 Mean flow in hexagonal convection: stability and nonlinear dynamics. *Physica D* **163**, 166.

Young, Y.-N., Riecke, H. & Pesch, W. 2003 Whirling hexagons and defect chaos in hexagonal non-Boussinesq convection. *New J. Phys.* **5**, 135.

Zhong, F. & Ecke, R. 1992 Pattern dynamics and heat transport in rotating Rayleigh-Bénard convection. *Chaos* **2**, 163.